Experimental Methodology and Theoretical Framework in Describing Constrained Plastic Flow of FCC Microscale Tensile Specimens

H.T. Vo[a], E.K. Still[a], K. Lam[a], A. Drnovšek[b], L. Capolungo[c], S.A. Maloy[c], P. Chou[d], P. Hosemann[a,*]

[a]University of California, Berkeley
[b]Jožef Stefan Institute, Jamova 39, 1000 Ljubljana, Slovenia
[c]Los Alamos National Laboratory, Materials Science Division
[d]Electric Power Research Institute

Abstract

Small scale mechanical testing (SSMT) allows for the quantification of the mechanical responses for microscale and nanoscale material volumes. It has significant potential in improving our fundamental understanding of plastic deformation and in providing an engineering solution for testing complex and/or critical materials. Importantly, previous studies have revealed that plastic intermittency, manifested as strain bursts, are characteristic of the plastic flow behavior at the small length scale. In this work, interfacial constraint has been utilized to suppress strain bursts in order to stabilize plasticity. A new parameter, blocked volume ratio (BVR), is introduced to quantify the degree of constraint for a microscale specimen due to an interface. We showed that the plastic flow behavior in FCC Ni-based metals is highly dependent on the BVR of the specimen.

Keywords: interfacial constraint; microscale testing; strain bursts; plastic intermittency

1. sssIntroduction

The introduction of small-scale mechanical testing (SSMT) by M. Uchic et al.[1] has enabled a thorough understanding of mechanical properties of materials at small length scales, from nanoscale to microscale [2–7]. With the ability to probe specific microstructural features and infer qualitative bulk properties from microscale tests, SSMT offers unparalleled practical advantages over conventional macroscale testing in many important industries such as nuclear power, micro-electro-mechanical system (MEMS) devices [8], and advanced coating [9]. Because of its significant potential for engineering applications, there has been an extensive amount of research dedicated to understanding mechanical properties at small length scales [1–15].

Past research suggest that the mechanical stress response of the micropillars/microtensile samples are susceptible to various extrinsic favors such as the sample dimensions [1,2,5,6,10–16], sample-aspect ratios [17,18], and experimental constraints [19–23]. While these studies have extended our understanding of the complexity of the mechanical response at the nano-to-micron length scale, they have also raised various questions that must be addressed in order to expand the capability of SSMT for engineering applications. In particular, numerous experimental and theoretical studies have revealed that strain bursts or plastic intermittency, caused by dislocation avalanches, are characteristic of the plastic flow behavior of microscale and nanoscale crystals [1,24–26]. These dislocation avalanche processes effectively suppress dislocation multiplication and strain hardening in small single crystal tests; in contrast, the large sample volume of the macroscale polycrystalline and single crystal experiments prevents dislocation starvation and allow sufficient dislocation interactions for strain hardening [27]. Furthermore, macroscopic-like necking [27] is not observed in microscale samples. With the exception of nanocrystalline or nanostructured materials, SSMT almost exclusively samples single crystal properties, and thus

measurements such as work hardening, total elongation, and ultimate tensile strength cannot be extrapolated to the bulk scale, hindering access plasticity related properties such as fracture mechanics on ductile materials at the small length scale. From the standpoint of the development of miniaturization of devices, strain bursts at the microscale can also lead to problems for the plastic forming of micro-size crystals [25]. Additionally, the plastic instability can increase the likelihood of sudden failure of miniaturized devices.

Recognizing the importance and the negative effects associated with strain busts, different research groups have investigated different strategies to suppress the strain burst behaviors [22,28–30] . The majority of these studies looks at the effect of passivation layers on thin films and microscale/nanoscale pillars. The common findings among these studies are that (1) the strain bursts can be suppressed by trapping dislocations using passivated layers, (2) the Bauschinger effect is present for passivated pillars and thin films, (3) the yield stress is higher for the passivated samples compared to the non-passivated samples. The major drawback of fully passivating the samples is that catastrophic failure, associated with large strain bursts, occurs when the passivated layer breaks during the deformation process [23] ; thus, it is not possible to suppress strain bursts in microscale tensile samples because the passivated layers (often an oxide layer or a ceramic coating) will break in tension loading. Additionally, fully coating the samples is problematic even when the coating does not break, for it impedes plastic deformation because the sample and the coating are in a parallel loading configuration (i.e. in order for the sample to plastically deform, the coated layer has to also deform to maintain geometric continuity). Our study proposes and validates a new experimental method to effectively suppress strain bursts in FCC nickel-based microtensile samples throughout the entire deformation process until failure. Furthermore, we have developed a new conceptual framework to validate our new experimental methodology. In this

work, we have uniquely incorporated the coupled effects of deformation by dislocation glide, crystal loading orientation, sample crystallinity, and sample dimensions into a single parameter, the blocked volume ratio (BVR), to describe the interfacial constraints on the plastic deformation behavior of FCC nickel-based microtensile samples. Our proposed framework aims to provide a new methodology to continue investigating the influence of interfacial constraints on microscale slip-dominated plastic deformation.

2. Theory

2.1. Block Volume Ratio

In the case of FCC, there are 12 independent slip systems that can contribute to dislocation-mediated plasticity. Generally, a slip system is activated when its resolved shear stress (RSS) overcomes the critical resolved shear stress (CRSS) required to initiate dislocation motion. Schmid's law is used to calculate the resolved shear stress along any given slip system as the product between the uniaxial applied stress and the slip system's Schmid factor

$$\tau_\alpha = \sigma_{applied} * m_\alpha \quad \text{Equation 1}$$

$$m_\alpha = \cos(\phi) * \cos(\lambda) \quad \text{Equation 2}$$

Where τ_α : the resolved shear stress along slip system α, $\sigma_{applied}$: uniaxial applied stress, m_α : Schmid factor of slip system α, ϕ : the angle between the loading direction and normal vector of the slip system, λ : the angle between the load direction and slip direction of the slip system.

To quantify the degree of constraint due to an interface for a given slip system, the concept of the *"blocked volume"* is introduced. The blocked volume of a slip system is defined as the volume where the slip planes intersect the constraining surface, so the dislocations are effectively pinned by the constraining surface. A numerical method using Python Scipy library [31] is used to calculate the blocked volume of a given slip system. The method uses the Quickhull algorithm

[32] to calculate the convex hull of the set of points belong in the blocked volume region. The method of introducing the set of points encapsulating the blocked volume region is detailed in Section 3.3. The calculated convex hull of the set of points gives the volume of the blocked region.

The blocked volume ratio (BVR) is defined as the ratio between the blocked volume over the total volume of a given sample. Different from the previous studies, the interfacial constraints in our study are partial constraints, as shown in Figure 1, hence the need for the BVR parameter. The two requirements for the external constraints are that the interface must be impermeable to dislocations and it also must remain intact during the deformation process until failure. The both requirements can be satisfied by selecting a strongly adhering coating of a different material or a grain boundary with a low cumulative transmission coefficient [33]. In general, the cumulative transmission coefficient can be used to estimate whether the grain boundary is a strong barrier to dislocation motion [34].

For a given crystal orientation and sample dimension, the general BVR analysis of FCC single crystal is demonstrated in Figure 1 and outlined as follows:

- Calculate the Schmid factors of all 12 slip systems using Schmid's law.
- Determine the corresponding BVR values by quantifying the blocked volume of the 12 slip systems, as illustrated in Figure 1 and explained in the Method section.
- If the BVR value of the slip system(s) of the highest Schmid factors is low (< 0.5), then strain burst is expected to take place along those systems regardless of the BVR of the other slip systems. The influence of the BVR value on the degree of constraint is elaborated in Section 2.2.
- If the BVR value of the primary slip systems is high (> 0.5), then the BVR values of the other slip systems are considered. The sample is effectively constrained when the

BVR values are high for all slip systems except for those of very low RSS values compared to the primary system(s), In other words, slip systems of very low RSS values are not expected to activate regardless of BVR values. For example, slip systems 4-6 have low BVR value of 0.191 and low Schmid factor values (0.127 and 0.253) so these slip systems are not expected to take place during the formation (Figure 1). The influence of the BVR value on the degree of constraint is elaborated in Section 2.2.

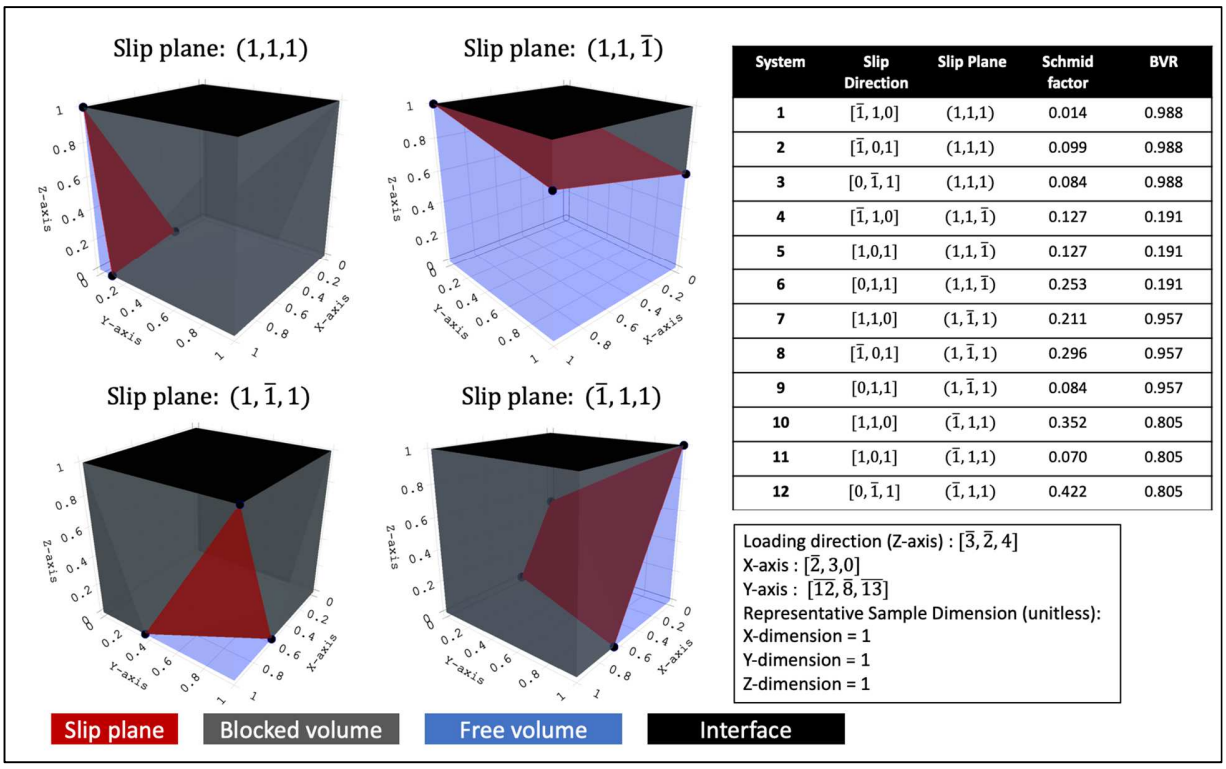

System	Slip Direction	Slip Plane	Schmid factor	BVR
1	[$\bar{1}$, 1,0]	(1,1,1)	0.014	0.988
2	[$\bar{1}$, 0,1]	(1,1,1)	0.099	0.988
3	[0, $\bar{1}$, 1]	(1,1,1)	0.084	0.988
4	[$\bar{1}$, 1,0]	(1,1, $\bar{1}$)	0.127	0.191
5	[1,0,1]	(1,1, $\bar{1}$)	0.127	0.191
6	[0,1,1]	(1,1, $\bar{1}$)	0.253	0.191
7	[1,1,0]	(1, $\bar{1}$, 1)	0.211	0.957
8	[$\bar{1}$, 0,1]	(1, $\bar{1}$, 1)	0.296	0.957
9	[0,1,1]	(1, $\bar{1}$, 1)	0.084	0.957
10	[1,1,0]	($\bar{1}$, 1,1)	0.352	0.805
11	[1,0,1]	($\bar{1}$, 1,1)	0.070	0.805
12	[0, $\bar{1}$, 1]	($\bar{1}$, 1,1)	0.422	0.805

Loading direction (Z-axis) : [$\bar{3}$, $\bar{2}$, 4]
X-axis : [$\bar{2}$, 3,0]
Y-axis : [$\bar{1}\bar{2}$, $\bar{8}$, $\bar{1}\bar{3}$]
Representative Sample Dimension (unitless):
X-dimension = 1
Y-dimension = 1
Z-dimension = 1

Figure 1. A BVR analysis for a representative FCC sample at given crystal orientation and dimension. The blocked volume visualization of all slip planes is shown. The blocked volume indicates the region where the slip plane intersects the constraining interface. The method of denoting the blocked volume is shown in Section 3.3. In similar fashion, the free volume indicates the region where the slip plane does not intersect the constraining interface. The slip planes

presented in the visualization are the slip planes that separate the free and the blocked volumes. The BVR values and Schmid factors of all slip systems are calculated.

2.2. Expected Influence of BVR on Dislocation-Mediated Plasticity in FCC metals

It is important to note at the outset that the following theory is developed for FCC single-crystal metals in which the major deformation mode is slip (i.e. deformation twinning is not considered.) By introducing the concept of the blocked volume, the single-crystal microtensile sample can be viewed as a bi-layer composite consisting of free and blocked volumes. Since the dislocation slip is constrained in the blocked volume while it is permitted in the free volume, the BVR value strongly influences the deformation behavior of the single crystal samplesUsing this approach, a single-crystal-sample's flow behavior can be categorized into three distinctly different regimes. Figure 2 outlines the three deformation modes corresponding to the three BVR value regimes. In Figure 2A,B,C, the blocked and free volume regions are indicated by the blue and the yellow areas, respectively. As introduced in Section 2.1, the blue region is where the slip planes intersect the constraining interface and the yellow region is where the slip planes do not intersect the constraining interface. The construction of the blocked and free volumes is shown in Section 3.3. In the blocked volume region, dislocations are pinned by the interface so no slip is permitted. In the free volume region, dislocations can escape to the free surfaces so slip is permitted. The first deformation regime, active at low BVR, is termed "*discrete slip band failure mode"*. The definition of the blocked volume guarantees that at a lower BVR, the active slip systems are relatively parallel to the constraining surface; therefore, the free volume and the blocked volume can be thought to be in a serial loading configuration, as shown in Figure 2A. This loading configuration implies that the free volume can deform by forming slip bands, independent from the blocked volume.

Increasing the BVR leads to the fact that the blocked volume is in a parallel loading configuration relative to the free volume, as seen in Figure 2B. This configuration is analogous to a bi-layer composite in parallel configuration. In this configuration, the free volume cannot deform independently from the blocked volume, and both have to accommodate the same strain in order to allow plastic deformation. Therefore, mixed mode deformation, characterized by simultaneous slip band formation in the free volume and necking behavior in the blocked volume, occurs in the parallel loading configuration. This deformation and failure regime at intermediate BVR is termed "*mixed mode*." A simple way to determine the loading configuration of the microtensile bar is if the boundary plane separating the free and blocked volumes intersects the base of the microtensile bar, then the sample is in a parallel loading configuration; otherwise, the sample is in a serial loading configuration. The transition between two loading configurations is expected to be around a BVR of 0.5, which is illustrated by the schematic of Figure 2B.

As the BVR of the active slip systems increase to a very high value, the tensile bar enters a mostly blocked configuration in which the blocked volume comprises the majority of the micro-tensile bar; thereby, only the blocked volume governs the deformation, as shown in Figure 2C. As a consequence, slip band formation is significantly suppressed. During the deformation process, the dislocations of the slip systems with the highest Schmid factor become mobile within the sample volumes, but they cannot escape the sample volume due to the constraining surface. As the stress increases, the other slip systems with sufficient RSS values also become active, leading to dislocation interaction among the different slip systems, which ultimately gives rise to strain hardening. After the work hardening stages, macroscopic-like necking is expected to set in, leading to failure. This deformation and failure mode is termed "*necking and strain hardening mode*". The

BVR value that marks the transition between "*mixed mode*" regime and "*necking and strain hardening mode*" regime is experimentally estimated in the Result section.

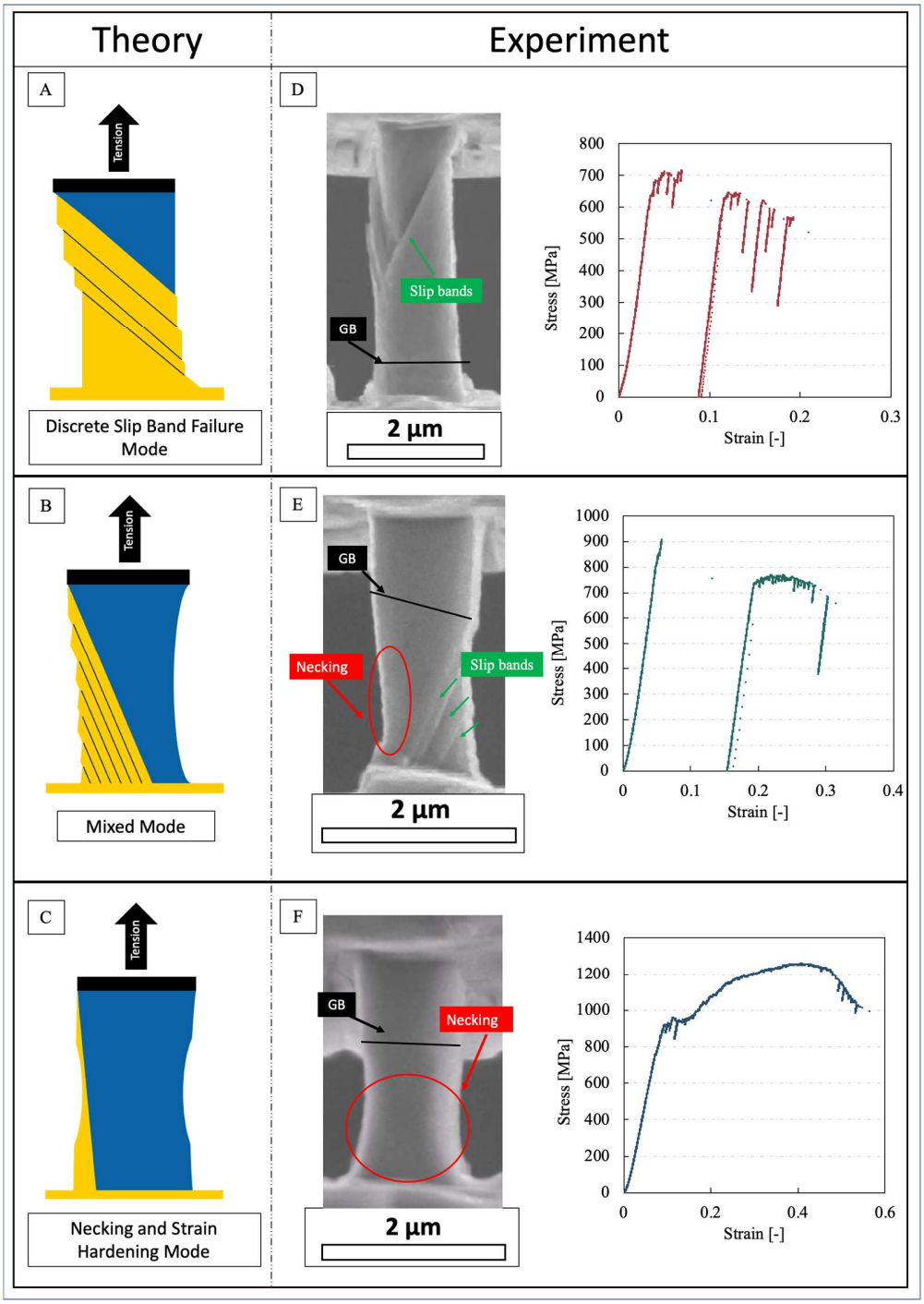

Figure 2. Schematics of (A) discrete slip band failure mode, (B) mixed mode, and (C) necking and strain hardening mode. Representative SEM images of the deformed samples and representative experimentally measured stress-strain curves measured experimentally are shown in (D) discrete

slip band failure mode, (E) mixed mode, and (F) necking and strain hardening mode. The free (unblocked) and blocked volumes of the primary slip system are denoted by yellow shading and blue shading, respectively.

3. Methods

3.1. Material Preparation

Pure Ni and Ni-based Alloy 600 are selected in our study. Pure Ni samples (99.99% purity) were mechanically polished to S_a=50 nm. The hard coating was deposited using a cathodic arc deposition system (Kobelco AIPocket). Prior to the deposition samples were heated to 400 °C and then ion etched in order to remove surface contamination. A power of 3 kW was used on each of four targets (Ti:Al = 50:50) at -70 V of bias voltage and a deposition pressure of 4 Pa. Pure N_2 gas was used to produce a nitride coating. The deposition time was set to 45 min, which resulted in 4 µm thick coatings on Ni samples mounted on a double rotation stage. The deposited TiAlN coating exhibits cubic structure and 32 GPa hardness. Afterwards several 500 µm long areas on the sample's side were ion cleaned with FIB (Helios Nanolab 650) in order to expose large Ni grains at the coating-substrate interface. For Nickel-based alloy 600, three thermal histories of the same heat were evaluated: solution annealed (SA), solution annealed and thermally treated (SATT), and mill annealed and cold-forged (MACF). The heat was received from the supplier in the mill-annealed (MA) condition (heat treated at 927 °C for 3.5 hours, water-quenched) and was subsequently cold forged (CF) to 15% deformation to produce the MACF condition. To produce the SA condition, the MA material was solution annealed at 1100 °C for a 0.5 h, followed by a water quench. Further thermal treatment of the SA material at 704 °C for 12 hours with a subsequent air quench produced the SATT condition. The materials were part of a larger effort to study the issue of intergranular stress corrosion cracking (IGSCC) of Ni-base Alloy 600 in the

primary water loop of pressurized water reactors. In this paper, only non-oxidized materials are discussed.

3.2. Microtensile Sample Fabrication

To understand the role of interfacial constraints on the plastic deformation behavior in FCC metals, we performed a series of microscale tensile tests as a function of the BVR parameter. Ni alloys with three distinct thermal treatments — solution-annealed (SA), solution-annealed thermally treated (SATT), and mill-annealed 15%-coldforged (MACF)— and pure Ni were tested with the constraining interface being grain boundaries and a ceramic coating, respectively. For ease of fabrication and testing, we used two different testing setups for the two constraint types.

A FEI Quanta 3D FEG SEM/FIB dual beam was utilized for the fabrication of microtensile specimens and for their subsequent testing. First, Electron Backscatter Diffraction (EBSD) was used to obtain crystal orientation information for grains of interest. The EBSD data allowed us to perform the BVR analysis in order to fabricate the microtensile samples with the desirable BVR. The microtensile tensile T-bone setup was used for the pure Ni samples with ceramic coating. The microtensile bars were fabricated using the focused Ga^{+}-ion beam according to the schematic in Figure 3. The sample width dimensions were between 1-2 μm and the sample's dimensional aspect-ratio was chosen based on the selected BVR. The rough milling was conducted at 30 keV with currents of 1-3 nA, and the final cleaning was performed at 0.3 nA. The same fabrication procedure was reported in [35].

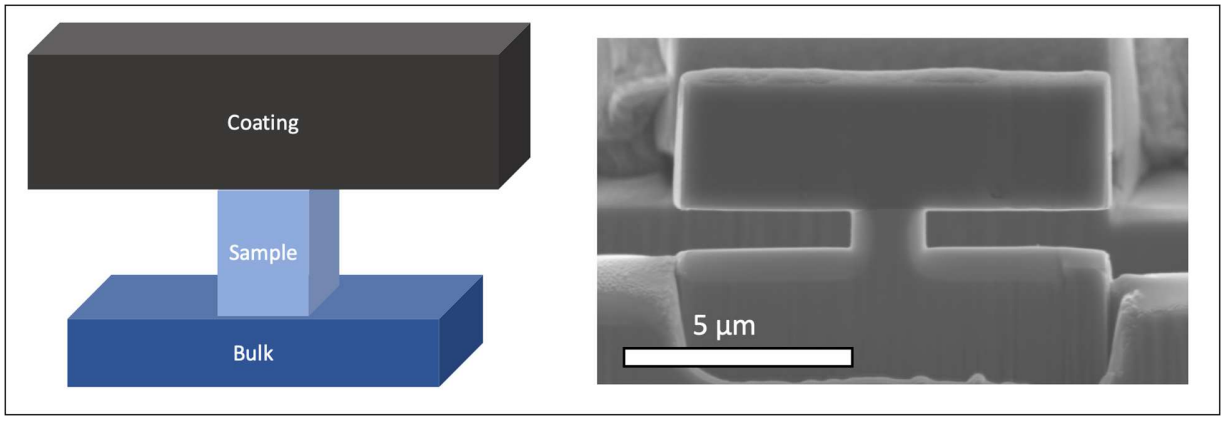

Figure 3. T-shape microtensile schematic and the SEM image of a representative tensile bar after fabrication.

A bicrystal tensile testing setup was used when a grain boundary was the constraining surface. Grain boundaries of low dislocation transmission probability were identified from the EBSD orientation map. The tensile bars containing such grain boundaries were then mounted on the Push-to-Pull device, manufactured by Bruker. Further thinning and cleaning of the tensile bar was done to obtain the final tensile dimensions, as shown in Figure 4. The detailed fabrication was reported in [36]. Since the grain of the lower BVR deforms while the other grain remains undeformed, the placement of the grain boundary in the tensile bar is carefully selected to obtain the desirable BVR values.. Table 1 lists the grain boundary angles, the corresponding cumulative transmission coefficients (λ), and the BVR values of the individual grains of the bicrystal samples. The λ values are calculated using the formulation proposed in [34]. A λ value of 12 means that the grain boundary is transparent to dislocation motion and a λ value of 0 means that the grain boundary is a perfect barrier.

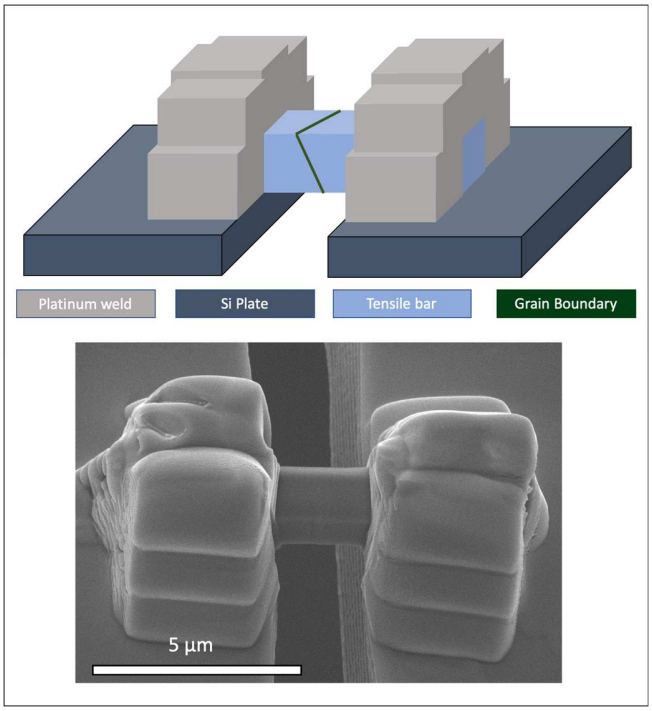

Figure 4. Bicrystal microscale tensile schematic and the SEM image of a representative tensile bar after fabrication.

Table 1. The misorientation angles, cumulative transmission coefficients λ, BVR values of the grains, and observed deformed grains.

Samples	Misorientation Angle (°)	λ	Grain 1 BVR	Grain 2 BVR	Deformed Grain
Ni Alloy, SA 1	59.7	2.951	0.0285	0.917	Grain 1
Ni Alloy, SA 2	54.4	0.641	0.808	0.666	Grain 2
Ni Alloy, SA 3	59.7	2.682	0.8334	0.776	Grain 2
Ni Alloy, SATT 1	42.1	1.027	0.218	0.95	Grain 1
Ni Alloy, SATT 2	43	0	0.932	0.841	Grain 2
Ni Alloy, MACF 1	48.2	1.087	0.667	0.298	Grain 2
Ni Alloy, MACF 2	38	0	0.921	0.867	Grain 2

Tensile tests were performed *in situ* in the SEM (Quanta 3D FEG) using the PI-88 Picoindenter, purchased from Bruker. The tests were conducted at a constant displacement rate of 10 nm/s, and the tensile bars were tested to failure. Videos of the *in situ* tests were recorded. Representative videos are shown in the Supplementary section (Videos 1,2,3).

3.3. Blocked Volume Calculation

While there are several ways to calculate the blocked volume, we present a simple yet versatile method. Given a list of vertex points defining the constraining surface and a 3D volume defined by a list of planar surfaces $[s_1, s_2, \dots]$, where each planar surface is a list of points defining the vertices of the surface $s_i = [(x_0, y_0, z_0), (x_1, y_1, z_1), \dots]$, the blocked volume is calculated by finding the set of points on the blocked volume and calculating the convex hull volume of those points. For each surface s_i, a grid of points G_i on the surface is calculated (Figure 5A). For a point p_i on the grid G_i, a slip plane L_i of the given slip system is defined by the tuple (p_i, v_n), where v_n is the normal vector of the slip plane (Figure 5B). If the plane L_i intersects the constraining surface, point p_i can be classified as "blocked" as it belongs to the blocked volume. The procedure is repeated for all points on all the free surfaces of the sample (Figure 5C). The convex hull volume of the set of these blocked points is the blocked volume for the slip system (Figure 5D). The developed method can also be applied to samples of cylindrical shapes.

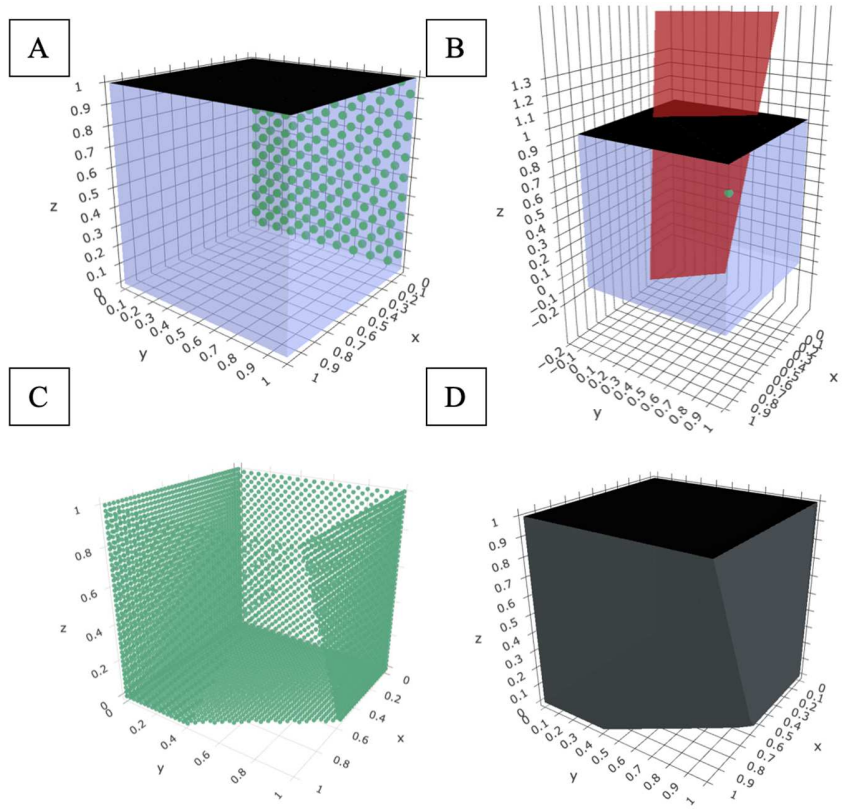

Figure 5. Visualization of the blocked volume calculation of the slip systems with slip plane $(1, \bar{1}, 1)$ *from Figure 1. A) A grid of points* G_i *(green circles) is calculated for each free surface* s_i*. B) For a point* p_i *(green circle) on the grid* G_i*, a slip plane* L_i *of the given slip plane (red plane) is defined by the tuple* (p_i, v_n)*, where* v_n *is the normal vector of the slip plane. If the plane* L_i *intersects the constraining surface (black plane), point* p_i *is classified as "blocked" as it belongs to the blocked volume. C) The procedure is repeated for all points on all the free surfaces of the sample to generate a full set of "blocked" points (green circles) on the free surfaces. D) The convex hull volume of the set of these blocked points is the blocked volume for the slip system (gray volume).*

4. Results

4.1. Experimental Validation for the FCC case

In order to correctly calculate the BVR value of each sample, the crystal orientation of the sample is selected such that the BVR value of the primary slip systems(s) is the lowest compared to all other slip systems with the exception of the very low RSS slip systems to ensure that the BVR of the primary slip system(s) is the limiting BVR value. An example of a sample with such crystal orientation is shown in Figure 1.

At low BVR values, "*discrete slip band failure mode*" was observed, as shown in Figure 2D. Supplementary Video 1 shows that the representative tensile bar of low BVR deforms by forming multiple bands until failure. The representative stress-strain curve (Figure 2D) shows multiple strain burst events, indicated by the large stain jumps, and no presence of work hardening after yielding. At intermediate BVR values, the tensile bars show "*mixed mode*" during deformation until failure, as shown in Figure 2E. During the deformation, slip bands formed in the free volume while necking took place in the blocked volume (Supplementary Video 2). The representative stress-strain curve (Figure 2E) shows a large strain jump, corresponding to simultaneous slip band formation and necking in the free and blocked volumes, respectively. At the very high BVR values, the tensile bars deform uniformly, followed by necking until failure, as shown in Figure 2F and Supplementary Video 3. The representative stress-strain curve of a high BVR test (Figure 2F) shows significant strain hardening and strong suppression of strain bursts in the stress-strain curve.

The deformation failure modes of all the tests are plotted against the BVR of the primary slip system(s) as shown in Figure 6. "*Mixed* mode" was observed for intermediate BVR values (0.67 and 0.78). At BVR values above 0.81, "*necking and strain hardening mode*" mode was observed. Experimentally, we set the estimate of the transition BVR value from "*mixed mode*" mode to "*necking and strain hardening mode*" to be 0.81 as it is the lowest BVR value measured

here which shows "*necking and strain hardening mode.*" However, one expects variabilities with the effectiveness of different constraint types for blocking slip. Also, it is important to note that there remain uncertainties associated with the measurements of the sample dimension and the crystal orientation, which affect the BVR calculation. Because of these uncertainties, the key takeaway from Figure 6 is that macroscopic deformation and failure mode can be obtained in FCC micro-tensile samples when the BVR values of the active slip systems are high.

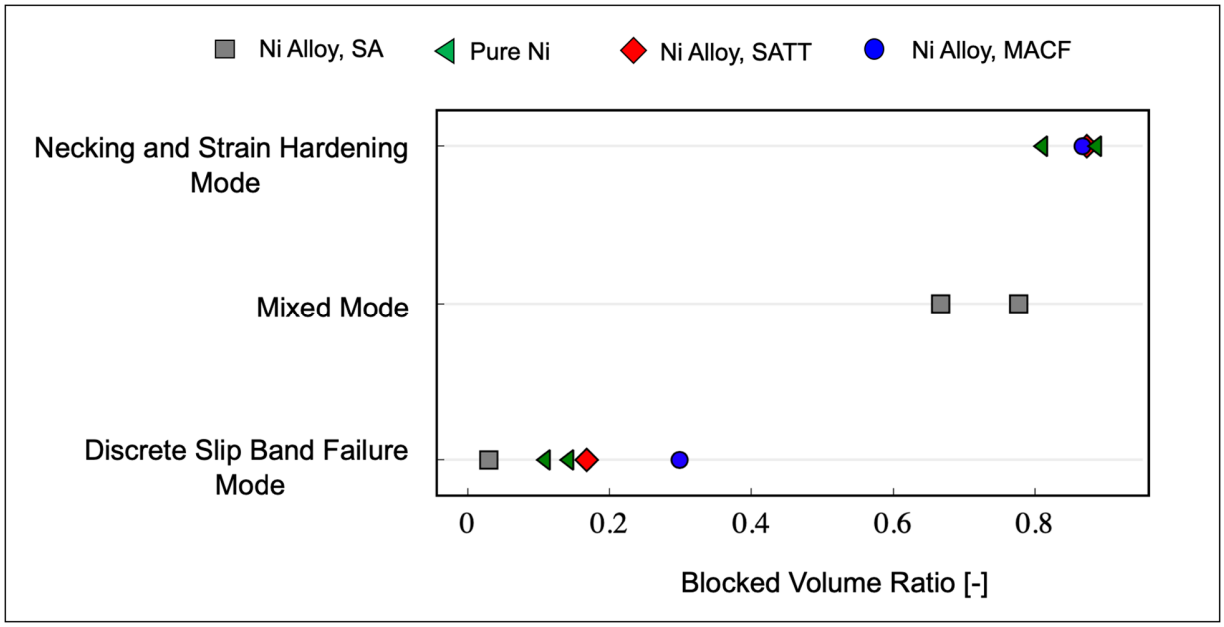

Figure 6. The deformation mode plotted versus the BVR of the primary slip systems

The experiments also demonstrated the flexibility of constraint type required to achieve macroscopic deformation. Figure 7 shows that the "*necking and strain hardening mode*" was observed in both microtensile testing of a T-shape tensile bar (Figure 7A) and a bicrystal tensile bars (Figure 7B) with the constraining interfaces to be the coating interface and grain boundary, respectively.

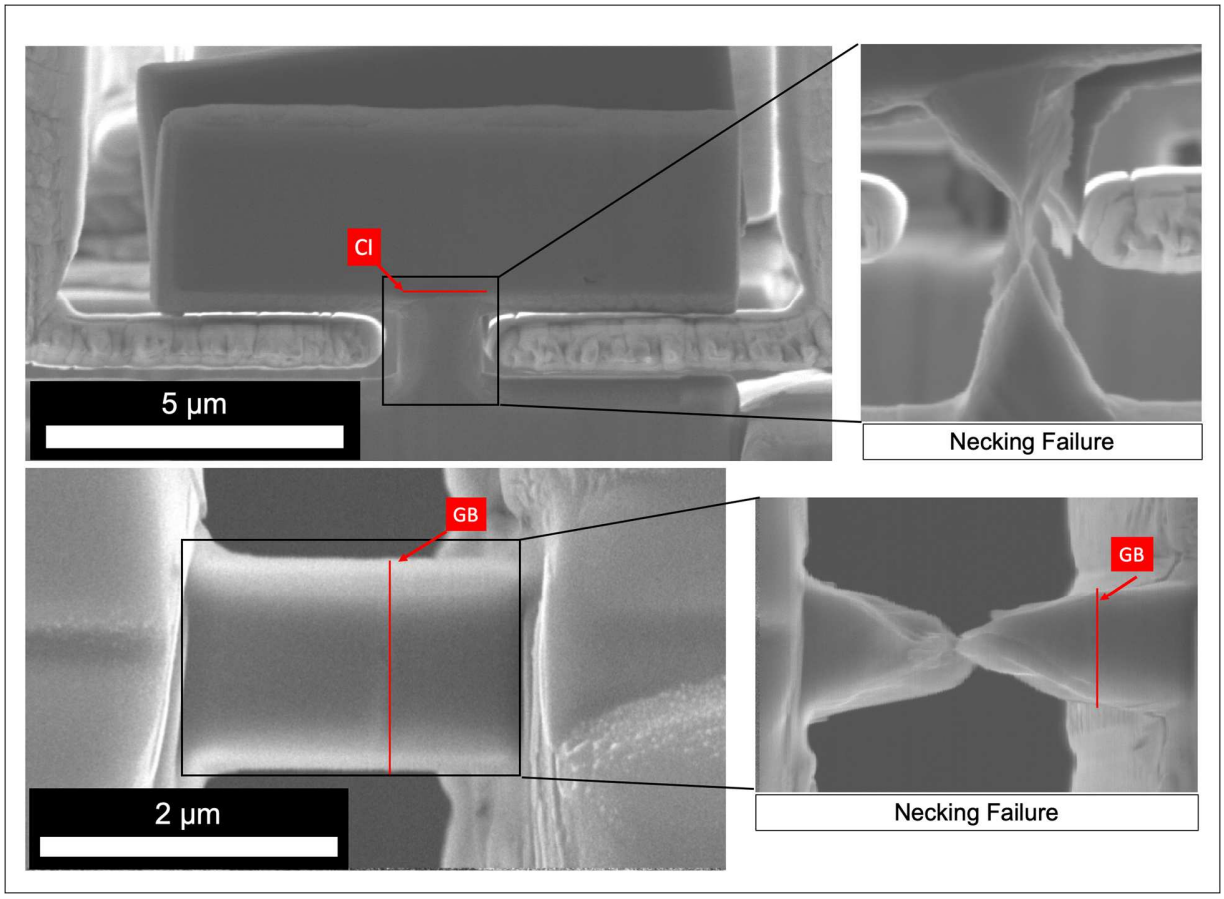

Figure 7. SEM images showing "necking and strain hardening mode" was observed for (A) the T-shape tensile testing setup and (B) the bicrystal tensile testing setup with the constraining interfaces being a coating interface (CI) and grain boundary (GB), respectively.

5. Discussion

Since the BVR of a sample depends on the crystal orientation and the height-to-width aspect ratio, the developed geometric criteria can be applied to create prediction maps for slip-dominated plastic deformation behavior in FCC crystals as a function of crystal orientation and aspect ratio. To demonstrate the usefulness of such a map, the multi-slip loading orientations – [001], [011], and [111] – are selected. Figure 8A, 8B, and 8C show the BVR considering a rectangular pillar in a FCC metal, whose top surface is the constraining surface, and the normal orientations of that top surface are taken to be [001], [110], and [111] respectively (determined by

Euler angles ϕ_2 and Φ), over a range of Euler angle ϕ_1 (0^o – 90^o) and height-to-width aspect ratio (0.5 – 5). The different deformation regimes ("*discrete slip band failure mode", "mixed mode"*, and "*necking and strain hardening mode"*) vary drastically for the three normal orientations. The color coding represents the lowest BVR values of the active slip systems for a given aspect ratio and crystal orientation. This type of mapping informs us about the potential influence of an interfacial interface on the plastic deformation behavior for any given crystal orientation and an aspect ratio. As shown in the figure, the microtensile samples of the crystal orientations and aspect ratios in the red and dark red regions (BVR > 0.811) are expected to undergo "*necking and strain hardening*" mode with mostly suppressed strain burst behavior. For the region whose BVR is below 0.5, "*discrete slip band formation*" mode and strain burst behaviors are expected. For FCC system whose major deformation mode is slip, the maps can inform on the expected deformation behavior in presence of an interfacial constraint. Additionally, compared to the previous studies [18,37,38], the BVR mapping over crystal orientations offers a new perspective on the influence of aspect ratio on the deformation behavior of the microscale experiments

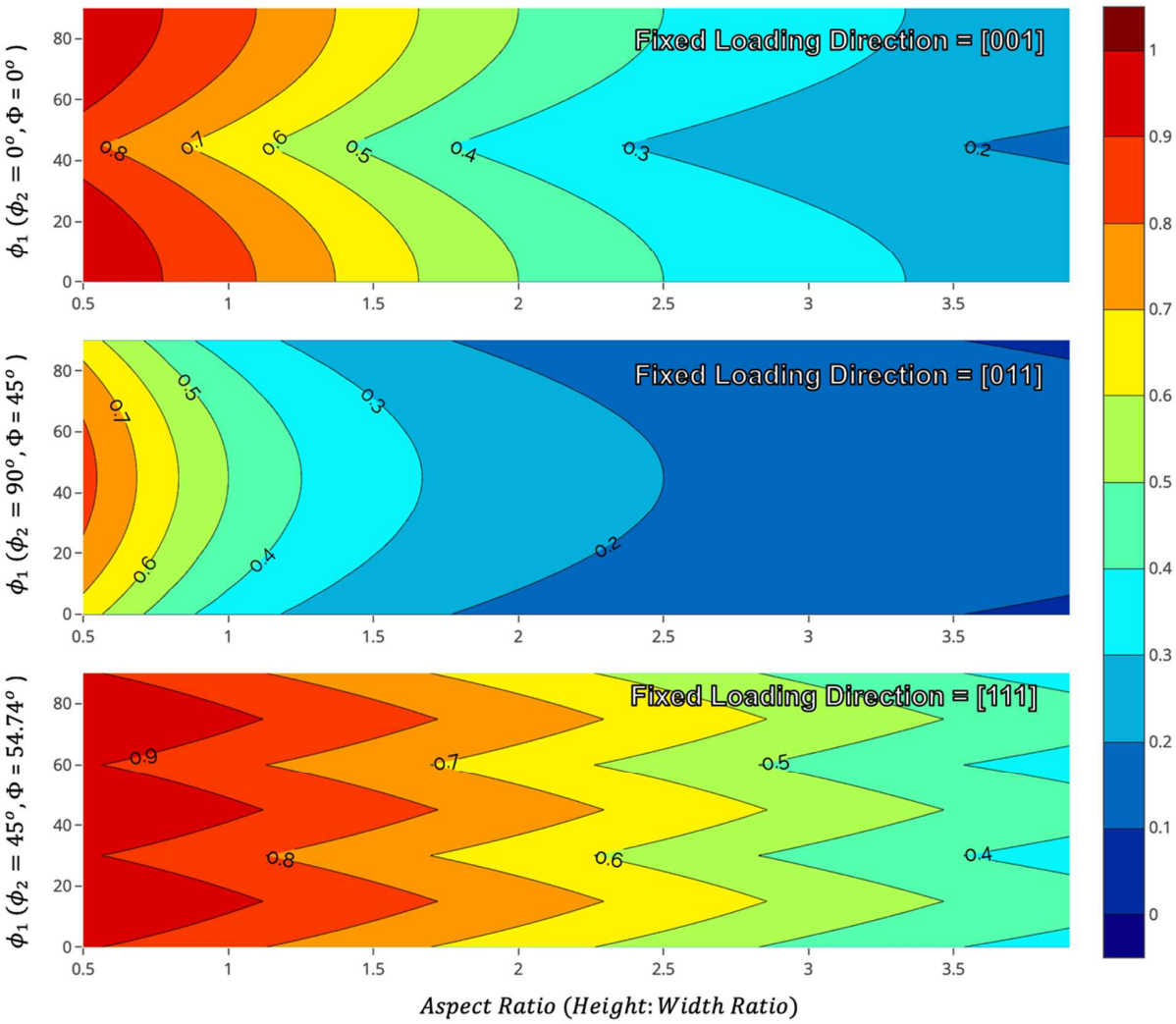

Figure 8. Mapping of the blocked volume ratio of FCC rectangular pillars for A) [001], B) [011], and C) [111] normal loading orientations over a range of Euler angle ϕ_1 (0^o – 90^o) and height-to-width aspect ratio (0.5 – 4). The color coding represents the lowest BVR values of the active slip systems for a given aspect ratio and crystal orientation.

Furthermore, the proposed theory motivates two research directions that deserve further exploration. The first direction is to examine whether the "necking and strain hardening" mode of high BVR samples is comparable with the plastic deformation of the same crystals at the macroscale. If it can be shown to be comparable with that of macroscopic deformation, it would

enable the ability to locally probe the macroscopic-like properties of individually build layers and identify the weak spots in additively manufactured metals and other advanced alloy designs across multiple disciplines. In addition, the nuclear industry can lower the cost of testing and reduce dose concerns by using microscale samples to obtain measurements that are relevant to large neutron-irradiated structural components as well as micrometer-thick ion-irradiated layers. However, several questions need to be addressed before we can realize this potential. Notably, the microstructural evolution and the dislocation density evolution between the microscale and macroscale tests must be compared. For instance, it is known that single crystal Ni forms dislocation cell structure [39] during macroscopic uniaxial testing. Therefore, one can see if the high BVR pure Ni samples would also form dislocation cell structure during microscale tensile testing. The second research direction is to use the proposed theory to enable future quantitative studies on grain boundaries and interfaces using small-scale testing. Important interfacial failure modes in alloys such as stress corrosion cracking [40], helium embrittlement [41], and hydrogen embrittlement [42] could be investigated and observed directly. One strategy is to manufacture microscale bicrystal tensile samples in which both grains have very high BVR values in order to suppress early plastic deformation of the matrix and encourage grain boundary failure.

6. Conclusion

Our work investigated the influence of interfacial constraint on the dislocation-mediated plasticity of FCC crystals in microscale tensile tests. We have introduced a simple yet effective parameter, BVR (blocked volume ratio), to quantify the degree of constraint for a given slip system due to an interface. Experimentally, we have shown that the plastic flow behavior is highly dependent on the BVR of the sample. Under the proposed framework, other important parameters (e.g. other slip systems, stacking fault energy, propensity for slip, dislocation cross-slip, and strain

rate) can be investigated to explore new phenomena and complexity. In our view, the BVR map provides a new and useful framework to understand and predict the active plastic deformation mode in microscopic samples. Additionally, the study provides future research directions which are important in further maturing SSMT. First, it introduces a new opportunity for research in extracting representative macroscopic properties of site-specific microstructural features of materials. Secondly, the blocked volume concept can be utilized to encourage interfacial failure by suppressing "discrete slip band failure mode" in the material adjacent to the interface. Therefore, it enables a direct examination of interfacial strength, such as grain boundaries, at the microscale. Important interfacial failure modes in alloys such as stress corrosion cracking, helium embrittlement, and hydrogen embrittlement can then be investigated through small scale testing.

Acknowledgement

The authors would like to acknowledge Electric Power Research Institute, Materials Aging Institute of Électricité de France , the DOE-NEUP program DE-NE 00008767, the Department of Energy National Nuclear Security Administration through the Nuclear Science and Security Consortium under Award Number DE-NA0003180. The authors acknowledge the Biomolecular Nanotechnology Center (BNC) facilities at UC Berkeley. Lastly, we acknowledge the CENN Nanocenter for the use of FIB.

Author Contribution Statement

H.T. Vo: Is the lead author, executed the experimental work, contributed to the BVR calculation, and proposed the initial Multi-Slip Constraint Model.

E. Still: Contributed to the experimental work by preparing FIB liftouts for bicrystal testing.

K. Lam: Lead the development of the code for the BVR analysis.

A. Drnovšek: Coated and prepared the pure Ni samples.

L. Capolungo: Contributed to the revision of the MSC model and the writing of the manuscript.

S.A. Maloy: Contributed to the revision of the MSC model and the writing of the manuscript.

P. Chou: Contributed to the development of the microtensile testing development via theoretical discussions.

P. Hosemann: Supervised the research and contributed to the revision of the MSC model and the writing of the manuscript.

Data availability

The data that support the findings of this study are available from the corresponding author upon reasonable request.

Code availability

The codes that support the findings of this study are available from the corresponding author upon reasonable request.

References

[1] M.D. Uchic, D.M. Dimiduk, J.N. Florando, W.D. Nix, Sample Dimensions Influence Strength and Crystal Plasticity, Science. 305 (2004) 986–989. https://doi.org/10.1126/science.1098993.

[2] D. Kiener, P. Hosemann, S.A. Maloy, A.M. Minor, *In situ* nanocompression testing of irradiated copper, Nat. Mater. 10 (2011) 608–613. https://doi.org/10.1038/nmat3055.

[3] P. Hosemann, Small-scale mechanical testing on nuclear materials: bridging the experimental length-scale gap, Scr. Mater. 143 (2018) 161–168. https://doi.org/10.1016/j.scriptamat.2017.04.026.

[4] Z.W. Shan, J. Li, Y.Q. Cheng, A.M. Minor, S.A. Syed Asif, O.L. Warren, E. Ma, Plastic flow and failure resistance of metallic glass: Insight from in situ compression of nanopillars, Phys. Rev. B. 77 (2008) 155419. https://doi.org/10.1103/PhysRevB.77.155419.

[5] M.D. Uchic, P.A. Shade, D.M. Dimiduk, Plasticity of Micrometer-Scale Single Crystals in Compression, Annu. Rev. Mater. Res. 39 (2009) 361–386. https://doi.org/10.1146/annurev-matsci-082908-145422.

[6] J.R. Greer, J.Th.M. De Hosson, Plasticity in small-sized metallic systems: Intrinsic versus extrinsic size effect, Prog. Mater. Sci. 56 (2011) 654–724. https://doi.org/10.1016/j.pmatsci.2011.01.005.
[7] S. Korte, W.J. Clegg, Micropillar compression of ceramics at elevated temperatures, Scr. Mater. 60 (2009) 807–810. https://doi.org/10.1016/j.scriptamat.2009.01.029.
[8] K.J. Hemker, W.N. Sharpe, Microscale Characterization of Mechanical Properties, Annu. Rev. Mater. Res. 37 (2007) 93–126. https://doi.org/10.1146/annurev.matsci.36.062705.134551.
[9] M. Sebastiani, K.E. Johanns, E.G. Herbert, F. Carassiti, G.M. Pharr, A novel pillar indentation splitting test for measuring fracture toughness of thin ceramic coatings, Philos. Mag. 95 (2015) 1928–1944. https://doi.org/10.1080/14786435.2014.913110.
[10] H. Tang, K.W. Schwarz, H.D. Espinosa, Dislocation escape-related size effects in single-crystal micropillars under uniaxial compression, Acta Mater. 55 (2007) 1607–1616. https://doi.org/10.1016/j.actamat.2006.10.021.
[11] J.R. Greer, W.D. Nix, Nanoscale gold pillars strengthened through dislocation starvation, Phys. Rev. B. 73 (2006) 245410. https://doi.org/10.1103/PhysRevB.73.245410.
[12] D.S. Gianola, C. Eberl, Micro- and nanoscale tensile testing of materials, JOM. 61 (2009) 24. https://doi.org/10.1007/s11837-009-0037-3.
[13] G. Dehm, Miniaturized single-crystalline fcc metals deformed in tension: New insights in size-dependent plasticity, Prog. Mater. Sci. 54 (2009) 664–688. https://doi.org/10.1016/j.pmatsci.2009.03.005.
[14] R. Dou, B. Derby, A universal scaling law for the strength of metal micropillars and nanowires, Scr. Mater. 61 (2009) 524–527. https://doi.org/10.1016/j.scriptamat.2009.05.012.
[15] A. Rinaldi, P. Peralta, C. Friesen, K. Sieradzki, Sample-size effects in the yield behavior of nanocrystalline nickel, Acta Mater. 56 (2008) 511–517. https://doi.org/10.1016/j.actamat.2007.09.044.
[16] C.R. Mayer, L.W. Yang, S.S. Singh, J. Llorca, J.M. Molina-Aldareguia, Y.L. Shen, N. Chawla, Anisotropy, size, and aspect ratio effects on micropillar compression of AlSiC nanolaminate composites, Acta Mater. 114 (2016) 25–32. https://doi.org/10.1016/j.actamat.2016.05.018.
[17] D. Kiener, W. Grosinger, G. Dehm, On the importance of sample compliance in uniaxial microtesting, Scr. Mater. 60 (2009) 148–151. https://doi.org/10.1016/j.scriptamat.2008.09.024.
[18] D. Kiener, W. Grosinger, G. Dehm, R. Pippan, A further step towards an understanding of size-dependent crystal plasticity: In situ tension experiments of miniaturized single-crystal copper samples, Acta Mater. 56 (2008) 580–592. https://doi.org/10.1016/j.actamat.2007.10.015.
[19] Y. Yang, J.C. Ye, J. Lu, F.X. Liu, P.K. Liaw, Effects of specimen geometry and base material on the mechanical behavior of focused-ion-beam-fabricated metallic-glass micropillars, Acta Mater. 57 (2009) 1613–1623. https://doi.org/10.1016/j.actamat.2008.11.043.
[20] D. Kiener, C. Motz, G. Dehm, Micro-compression testing: A critical discussion of experimental constraints, Mater. Sci. Eng. A. 505 (2009) 79–87. https://doi.org/10.1016/j.msea.2009.01.005.

[21] D. Raabe, D. Ma, F. Roters, Effects of initial orientation, sample geometry and friction on anisotropy and crystallographic orientation changes in single crystal microcompression deformation: A crystal plasticity finite element study, Acta Mater. 55 (2007) 4567–4583. https://doi.org/10.1016/j.actamat.2007.04.023.
[22] K.S. Ng, A.H.W. Ngan, Effects of trapping dislocations within small crystals on their deformation behavior, Acta Mater. 57 (2009) 4902–4910. https://doi.org/10.1016/j.actamat.2009.06.053.
[23] A.T. Jennings, C. Gross, F. Greer, Z.H. Aitken, S.-W. Lee, C.R. Weinberger, J.R. Greer, Higher compressive strengths and the Bauschinger effect in conformally passivated copper nanopillars, Acta Mater. 60 (2012) 3444–3455. https://doi.org/10.1016/j.actamat.2012.03.013.
[24] D.M. Dimiduk, C. Woodward, R. LeSar, M.D. Uchic, Scale-Free Intermittent Flow in Crystal Plasticity, Science. 312 (2006) 1188–1190. https://doi.org/10.1126/science.1123889.
[25] F.F. Csikor, C. Motz, D. Weygand, M. Zaiser, S. Zapperi, Dislocation Avalanches, Strain Bursts, and the Problem of Plastic Forming at the Micrometer Scale, Science. 318 (2007) 251–254. https://doi.org/10.1126/science.1143719.
[26] M.-C. Miguel, A. Vespignani, S. Zapperi, J. Weiss, J.-R. Grasso, Intermittent dislocation flow in viscoplastic deformation, Nature. 410 (2001) 667–671. https://doi.org/10.1038/35070524.
[27] S.D. Antolovich, R.W. Armstrong, Plastic strain localization in metals: origins and consequences, Prog. Mater. Sci. 59 (2014) 1–160. https://doi.org/10.1016/j.pmatsci.2013.06.001.
[28] L. Nicola, Y. Xiang, J.J. Vlassak, E. Van der Giessen, A. Needleman, Plastic deformation of freestanding thin films: Experiments and modeling, J. Mech. Phys. Solids. 54 (2006) 2089–2110. https://doi.org/10.1016/j.jmps.2006.04.005.
[29] Y. Xiang, J.J. Vlassak, Bauschinger effect in thin metal films, Scr. Mater. 53 (2005) 177–182. https://doi.org/10.1016/j.scriptamat.2005.03.048.
[30] Y. Xiang, J.J. Vlassak, Bauschinger and size effects in thin-film plasticity, Acta Mater. 54 (2006) 5449–5460. https://doi.org/10.1016/j.actamat.2006.06.059.
[31] T.E. Oliphant, Python for Scientific Computing, Comput. Sci. Eng. 9 (2007) 10–20. https://doi.org/10.1109/MCSE.2007.58.
[32] C.B. Barber, D.P. Dobkin, D.P. Dobkin, H. Huhdanpaa, The Quickhull Algorithm for Convex Hulls, ACM Trans Math Softw. 22 (1996) 469–483. https://doi.org/10.1145/235815.235821.
[33] E. Bayerschen, A.T. McBride, B.D. Reddy, T. Böhlke, Review on slip transmission criteria in experiments and crystal plasticity models, J. Mater. Sci. 51 (2016) 2243–2258. https://doi.org/10.1007/s10853-015-9553-4.
[34] E. Werner, W. Prantl, Slip transfer across grain and phase boundaries, Acta Metall. Mater. 38 (1990) 533–537. https://doi.org/10.1016/0956-7151(90)90159-E.
[35] H.T. Vo, A. Reichardt, D. Frazer, N. Bailey, P. Chou, P. Hosemann, In situ micro-tensile testing on proton beam-irradiated stainless steel, J. Nucl. Mater. 493 (2017) 336–342. https://doi.org/10.1016/j.jnucmat.2017.06.026.
[36] C. Howard, C.D. Judge, P. Hosemann, Applying a new push-to-pull micro-tensile testing technique to evaluate the mechanical properties of high dose Inconel X-750, Mater. Sci. Eng. A. 748 (2019) 396–406. https://doi.org/10.1016/j.msea.2019.01.113.

[37] C.P. Frick, B.G. Clark, S. Orso, A.S. Schneider, E. Arzt, Size effect on strength and strain hardening of small-scale [111] nickel compression pillars, Mater. Sci. Eng. A. 489 (2008) 319–329. https://doi.org/10.1016/j.msea.2007.12.038.
[38] H. Zhang, B.E. Schuster, Q. Wei, K.T. Ramesh, The design of accurate micro-compression experiments, Scr. Mater. 54 (2006) 181–186. https://doi.org/10.1016/j.scriptamat.2005.06.043.
[39] A.S. Schneider, D. Kiener, C.M. Yakacki, H.J. Maier, P.A. Gruber, N. Tamura, M. Kunz, A.M. Minor, C.P. Frick, Influence of bulk pre-straining on the size effect in nickel compression pillars, Mater. Sci. Eng. A. 559 (2013) 147–158. https://doi.org/10.1016/j.msea.2012.08.055.
[40] A. King, G. Johnson, D. Engelberg, W. Ludwig, J. Marrow, Observations of Intergranular Stress Corrosion Cracking in a Grain-Mapped Polycrystal, Science. 321 (2008) 382–385. https://doi.org/10.1126/science.1156211.
[41] M.I. Baskes, Recent Advances in Understanding Helium Embrittlement in Metals, MRS Bull. 11 (1986) 14–18. https://doi.org/10.1557/S0883769400069116.
[42] S. Bechtle, M. Kumar, B.P. Somerday, M.E. Launey, R.O. Ritchie, Grain-boundary engineering markedly reduces susceptibility to intergranular hydrogen embrittlement in metallic materials, Acta Mater. 57 (2009) 4148–4157. https://doi.org/10.1016/j.actamat.2009.05.012.